# Scanning probe spectroscopy of sulfur vacancies and $MoS_2$ monolayers in side-contacted van der Waals heterostructures

To cite this article: K Nisi *et al* 2025 *2D Mater.* **12** 015023

IOP Publishing 2D Mater. 12 (2025) 015023 https://doi.org/10.1088/2053-1583/ada046

2D Materials



PAPER

# Scanning probe spectroscopy of sulfur vacancies and $MoS_2$ monolayers in side-contacted van der Waals heterostructures

K Nisi[1,2,3], J C Thomas[3], S Levashov[1], E Mitterreiter[1,2], T Taniguchi[4], K Watanabe[5], S Aloni[3], T R Kuykendall[3], J Eichhorn[1], A W Holleitner[1,2], A Weber-Bargioni[3] and C Kastl[1,2,*]

[1] Walter Schottky Institute and Physics Department, Technical University of Munich, Am Coulombwall 4a, 85748 Garching, Germany
[2] Munich Center for Quantum Science and Technology (MCQST), Schellingstraße 4, 80799 Munich, Germany
[3] Molecular Foundry, Lawrence Berkeley National Laboratory, Berkeley, CA 94720, United States of America
[4] Research Center for Materials Nanoarchitectonics, National Institute for Materials Science, 1-1 Namiki, Tsukuba 305-0044, Japan
[5] Research Center for Electronic and Optical Materials, National Institute for Materials Science, 1-1 Namiki, Tsukuba 305-0044, Japan
[*] Author to whom any correspondence should be addressed.

**E-mail:** christoph.kastl@wsi.tum.de

**Keywords:** TMDC, scanning tunneling microscopy, conductive atomic force microscopy, defects, van der Waals heterostructure

Supplementary material for this article is available online

OPEN ACCESS

RECEIVED
28 August 2024

REVISED
11 December 2024

ACCEPTED FOR PUBLICATION
17 December 2024

PUBLISHED
30 December 2024



## Abstract

We investigate the interplay between vertical tunneling and lateral transport phenomena in electrically contacted van der Waals heterostructures made from monolayer $MoS_2$, hBN, and graphene. We compare data taken by low-temperature scanning tunneling spectroscopy to results from room-temperature conductive atomic force spectroscopy on monolayer $MoS_2$ with sulfur vacancies and with varying hBN layers. We show that for thick hBN barrier layers, where tunneling currents into the conductive substrate are suppressed, a side-contact still enables addressing the defect states in the scanning tunneling microscopy via the lateral current flow. Few-layer hBN realizes an intermediate regime in which the competition between vertical tunneling and lateral transport needs to be considered. The latter is relevant for device structures with both a thin tunneling barrier and a side-contact to the semiconducting layers.

Two-dimensional (2D) van der Waals heterostructures possess promising characteristics for next-generation (opto)electronic devices [1, 2]. Vertical heterostructures, with van der Waals layers assembled to form atomically well-defined, ultra-thin tunneling devices, can leverage the particular advantages of the 2D materials platform, overcoming fundamental limits of conventional device architectures [3] and providing new functionality for applications in quantum technologies [4, 5]. These 2D heterostructures typically consist of atomically thin highly-conductive electrodes (e.g. graphene), insulating barriers (e.g. few-layer hBN), and monolayer semiconductors (e.g. $MoS_2$, $WS_2$, $MoSe_2$ or $WSe_2$). The wide-gap insulator hBN has proven to be an excellent tunneling barrier in vertical device structures [6, 7]. Its low defect density [6] and high dielectric breakdown strength [8, 9] allow fabricating barriers which are only a few angstroms thick and can be used to fine tune non-equilibrium tunneling currents, electron-hole interactions, and equilibrium charge transfer between two neighboring layers [6, 10].

Moreover, the 2D van der Waals heterostructures allow incorporating various defects as single-photon sources directly integrated into the device architecture [11]. For example, vacancy defects [12] in monolayer transition metal dichalcogenides can be implanted into tunneling circuits [13] with nanometer precision using ion beam patterning [14, 15]. For an atomic defect to be an effective two-level system, it is crucial to reduce the degeneracies of its ground and excited states, which can be achieved in defect complexes with lowered symmetries or in charged defects [16, 17]. In this context, recent scanning tunneling microscopy (STM) studies on sulfur vacancies in monolayer $MoS_2$ have directly resolved the spontaneous symmetry lowering of the vacancy's defect orbitals upon charging, known as

the Jahn–Teller distortion [18–20]. Both experiment and theory demonstrate significant energetic corrections (10 s of meV) at the single particle level [18–22]. However, so far, these STM studies only considered defects in $MoS_2$ layers which are supported directly on a graphene [18–20] or gold substrate [23]. In that case, the (semi)-metallic substrate not only induces substantial charge transfer into the monolayer semiconductor [24], but it also quenches the optical emission from the relatively long-lived, localized defect excitons [25], while emission from the fast free exciton is still detectable. Therefore, a direct correlation between the single particle defect orbitals typically resolved by STM of transition metal dichalcogenides on graphene and the excitonic defect states revealed by optical spectroscopy of $MoS_2$ on insulating hBN remains challenging. An insulating hBN barrier can potentially provide the necessary decoupling of the semiconducting $MoS_2$ layer and thus of the point defects from the metallic graphene. Ultimately, such a heterostructure facilitates resolving localized exciton transition at the atomic scale via tip-induced luminescence [26–28]. The latter approach has been successfully applied to molecules on metal surfaces, where a thin insulating barrier, typically few layers of single crystal salt, provides the necessary decoupling from the substrate [29].

In this work, we present scanning probe measurements of $MoS_2$/hBN heterostructures with sulfur vacancy defects. We employ scanning tunneling spectroscopy (STS) at 4 K to gain insights into the electronic properties of the heterostructures. A challenge in such experiments is the identification of their respective locations on the same heterostructure using the limited scan range and limited coarse positioning accuracy available in the STM. Therefore, we utilize conductive atomic force microscopy (cAFM) at room temperature as a complementary tool to characterize the charge transport for different heterostructure configurations with varying hBN thickness on the same sample. To characterize also thick decoupling barriers, where vertical tunneling is suppressed, we rely on side-contacted heterostructures, where the lateral current flow enables electronic spectroscopy of the localized states.

## 1. Results

Thin layers of hBN (down to a monolayer) and monolayers (ML) of $MoS_2$ were prepared via micromechanical cleavage and placed onto an epitaxially-grown graphene on *(6H)*-SiC substrate via a stamping procedure (see Methods). The layers were stacked to create different regions of interest within one sample. Specifically, we investigated the following heterostructure configurations: i) hBN on epitaxial graphene (EG), ii) $MoS_2$ on hBN on EG, and iii) $MoS_2$ on EG. Importantly, the $MoS_2$ layer was contacted directly to the graphene substrate via a side-contact to ensure a conductive pathway even for thick hBN barriers, where direct vertical tunneling is suppressed. In other studies, similar side-contacts were achieved via gold or nanopatterned graphene electrodes [30, 31]. The heterointerfaces were probed by scanning probe microscopy and spectroscopy with the bias applied between the EG and the tip (figure 1(a)). We studied the properties, in particular the charging state and in-gap states, of single sulfur vacancy defects (indicated exemplarily by the black circles in figure 1(a)) in the $MoS_2$ monolayer for the different layer configurations. Figure 1(b) shows a helium ion microscope image of such a heterostructure sample. Due to the high material contrast of He-ion microscopy, all layers are visible enabling the assessment of the exact position of each material, including microcracks in the layers. The different materials are labeled accordingly. For this particular sample, the ML $MoS_2$ is divided in three regions (on thick hBN, on ML hBN, and directly on EG/SiC).

In our STM measurements, the coarse position of the sample with respect to the tip was identified via an optical access port. Gold contacts and other bulk crystals in close vicinity to the heterostructure served as optical reference markers for the approach of the tip. To identify the different locations on the sample, we relied on STS and STM images. Hereby, distinctive features such as lattice constants and defects support STS measurements to enable the assignment of each area (figure S1). Figures 1(c) and (d) depict representative low-temperature STS measurements for different areas on the heterostructure. The $dI/dV$ curves were recorded with a modulation voltage AM = 5 mV and a current setpoint of $I_{set}$ = 150 pA. For each configuration, we recorded spectra on multiple locations and determined averaged values for the band onsets.

For $MoS_2$ directly on graphene (figure 1(c)), the onsets of the tunneling current appear at +0.64 V and −1.76 V corresponding to the conduction band minimum (CBM) and valence band maximum (VBM) of $MoS_2$. This simple analysis translates into an estimated value of the bandgap of 2.4 eV. The bandgap in previous reports varies between 2 and 2.5 eV [14, 30, 32, 33]. Nevertheless, an exact determination of the bandgap value is difficult and requires a more careful analysis as described, for example, by Murray *et al* [32]. This is due to the fact that the tunneling current near the $\Gamma$-point is typically enhanced compared to the K-point [34], because states with finite in-plane momentum decay faster into the vacuum [35]. The Fermi level is not mid-gap but shifted towards the CBM, which we assign to the charge transfer from the graphene [16]. When decoupling the $MoS_2$ with hBN (figure 1(d)), we observe two effects. First, the onset of the CBM shifts systematically to higher voltages (on average we find +0.4 eV), suggesting either a

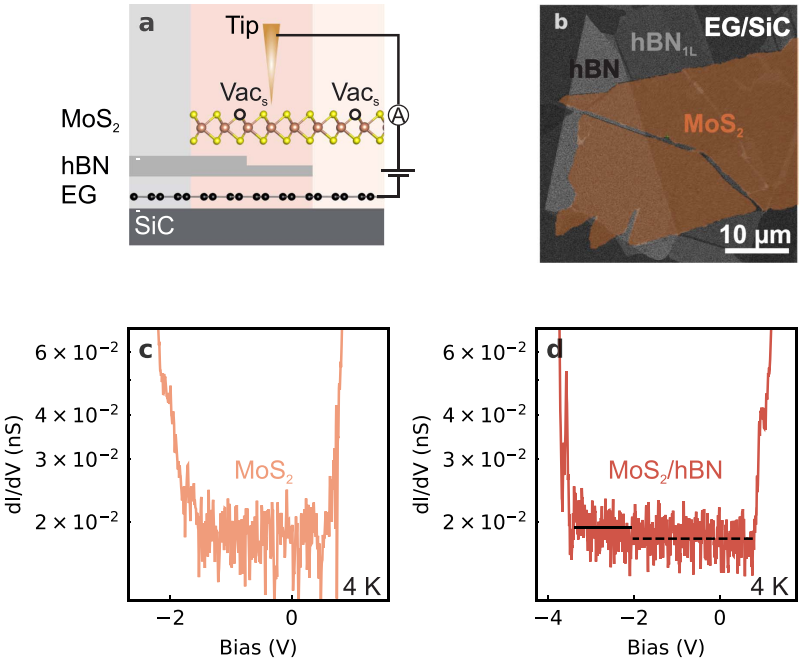


**Figure 1.** Sample scheme and tunneling process. (a) hBN and ML $MoS_2$ are placed on epitaxial graphene (EG) on SiC. The different heterointerfaces and sulfur vacancies ($Vac_s$) in the $MoS_2$ layer are probed by STS at $T = 4$ K using a tungsten tip prepared on a gold substrate. (b) False-colored helium ion microscope image of the $MoS_2$/hBN/EG heterostructure revealing the different layer configurations (beam current 170 fA, acceleration voltage 30 kV, FOV 40 × 40 $\mu m^2$, scan dwell time 2 $\mu s$). (c) Low-temperature scanning tunneling spectroscopy measurements of ML $MoS_2$ directly on EG/SiC and (d) ML $MoS_2$ decoupled from the EG/SiC via a hBN tunneling barrier. The dashed line marks the median of the noise level around 0 V. The solid black line marks the median signal below −2 V. The noticeable increase of the signal at voltages below −2 V is interpreted as the onset of the valence band in the $MoS_2$/hBN heterostructure. Tunneling spectra are slightly offset to avoid negative values in the log-plot.

reduced charge transfer from the graphene or a possible combination of strain and screening resulting in overall band gap renormalization [36]. Second, tunneling currents into the valence band of the $MoS_2$ appear to be suppressed below the noise level of our measurement (dashed black lines in figure 1(d)). Only at bias voltages below −3.68 V, which we tentatively assign to the VBM onset in hBN (cf. supporting information figure S2), the tunneling current increases noticeably. Averaging the signal below (solid black line in figure 1(d)) and above (dashed black line in figure 1(d)) the expected value of the VBM of $MoS_2$, the spectrum reveals a small, but finite increase inside the gap reminiscent of the VBM in $MoS_2$ as indicated by the black solid line in figure 1(d). The fact that the gap of $MoS_2$ is not properly resolved points towards the possibility that we probe ML $MoS_2$ on bulk (∼22 nm) hBN, rather than on ML hBN, via the side-contact. However, we note that it is difficult to identify the thickness of the underlying hBN based on STS alone.

To get a better understanding of the underlying charge transport processes, we performed complementary cAFM measurements at room temperature under inert gas atmosphere ($N_2$) on the above heterostructure and on different flakes of varying thickness lying in close vicinity. We determined the position of each measurement and corresponding layer thickness by AFM maps and height profiles (cf. figures S3 and S4). Areas of interest for cAFM (2 × 2 $\mu m^2$) were cleaned with an AFM tip using contact mode to remove residual adsorbates from the exposure to ambient (cf. figures S5 and S6 and Methods) [37]. For the *IV*-spectroscopy, the contact force was kept as small as possible, but large enough to enable good electric contact. Nevertheless, when comparing STS at low temperature and cAFM measurements at room temperature, one needs to keep in mind that for the latter, the tip is in physical contact with the sample surface, i.e. the tip enters the repulsive regime of tip-sample interaction during the current measurement. Hence, the *IV*-curves recorded in cAFM typically do not reveal the density of states as in STS, unless a thin, insulating tunneling barrier is introduced between the AFM tip and the material under test [38].

Figure 2(a) depicts layer-dependent *IV*-curves (semi-log scale) of insulating hBN on EG. As expected, the overall current amplitude at a given voltage drops with increasing barrier height or hBN layer number [10]. Large tunneling currents (nA-regime) are observed for barrier heights up to three layers, most probably dominated by the conductive character of the underlying graphene [38]. For six layers of hBN, direct tunneling is suppressed and only at very high bias magnitudes, we observe small currents (pA-regime). For better comparison to STS, figure 2(b) shows the numerically derived $\Delta I/\Delta V$ spectra measured by cAFM. The spectra for ML and

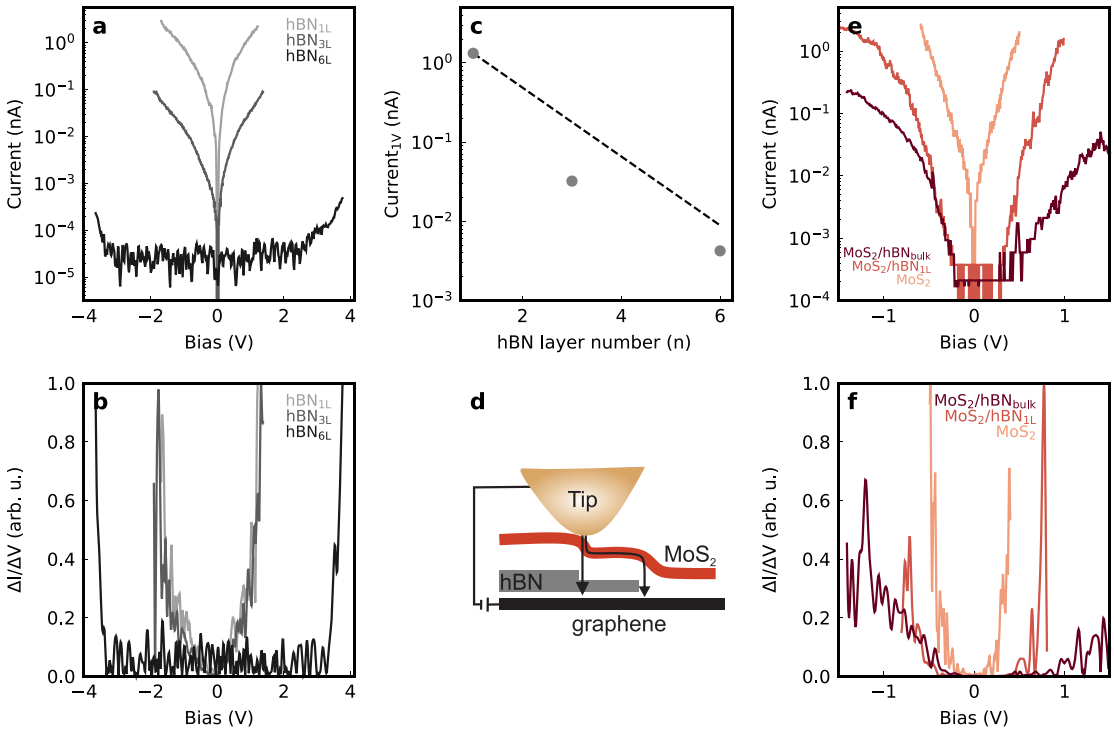


**Figure 2.** Conductive AFM spectroscopy. (a) Absolute value of the cAFM current for three hBN/EG heterointerfaces with a monolayer (light gray), trilayer (dark gray), and hexalayer (black) hBN barrier. Significant tunneling currents through the gap of hBN are resolved for monolayer and trilayer hBN. (b) Normalized conductance $\Delta I/\Delta V$ numerically derived from the data in (a). (c) Current at a bias of 1 V ($\text{Current}_{1V}$) extracted from the data in (a) as a function of hBN layer number. The dashed line is the theoretical scaling of the exponential decay assuming an ideal tunneling process through a hBN barrier with given layer number. (d) Sketch of the vertical and lateral current pathways (arrows) in the side-contacted $MoS_2$ heterostructure. (e) Absolute value of the cAFM current for different heterostructure configurations: $MoS_2$ supported directly on EG/SiC (orange), $MoS_2$ with an additional ML hBN barrier (light red), and $MoS_2$ on bulk hBN (dark red). Lateral transport is dominant for $MoS_2$ on bulk hBN (dark red), whereas it is negligible for $MoS_2$ directly on EG (orange). (f) Normalized conductance $\Delta I/\Delta V$ numerically derived from the data in (c).

trilayer hBN are virtually identical after normalization, pointing towards a predominant direct tunneling current through the thin barrier layer. The suppression of the tunneling current, extracted at a fixed bias of 1 V, with barrier thickness is shown in figure 2(c). The dashed line is the naively expected exponential scaling law assuming an ideal tunneling process through a hBN barrier with given layer number. Tentatively, we fit the data with an exponential decay, giving a decay constant of 1.1 $Å^{-1}$, similar to previous literature [39]. Note that when very large contact forces are used (on the order of hundreds of nN), the applied pressure can further modify the tunneling current due to the local indentation of the van der Waals stack [40]. To ensure maximum comparability within this work, we kept the applied force small ($\sim$1 nN) such that any local indentations are expected to be negligible.

Next, cAFM measurements were conducted on the side-contacted $MoS_2$ monolayer with different thicknesses of hBN below. Depending on the hBN thickness, vertical tunneling through $MoS_2$ and hBN, lateral current flow through the $MoS_2$ or a combination of both have to be considered (figure 2(d)). For $MoS_2$ probed in an area where it is directly supported on EG (orange curve, figures 2(e) and (f)), we observe high currents (nA-regime) already close to zero bias, suggesting direct tunneling through the ML $MoS_2$ barrier into graphene [40]. For $MoS_2$ on bulk hBN (dark red curves in figures 2(e) and (f)), the vertical tunneling is expected to be completely suppressed with barrier widths far above the tunneling limit (cf. figure 2(c)). Then, the current flow from $MoS_2$ to graphene is expected to proceed exclusively via a lateral drift-diffusion process. The resulting $IV$-curves can be interpreted as a lateral device with a Au/$MoS_2$ Schottky-contact and an efficient, vertical $MoS_2$/graphene junction in series (figure 2(d)). $MoS_2$ on ML hBN seems to be in-between the direct tunneling and the lateral transport scenario (red curves in in figures 2(e) and (f)). In other words, lateral transport and vertical tunneling provide two competing current pathways in the investigated samples with electrical side-contacts. Consequently, the difference in current between the three different configurations at identical bias gives an idea of lateral and tunnel contribution at room temperature. As a control experiment, we removed the side-contact of $MoS_2$ on bulk hBN by nano-mechanical manipulation using the AFM tip. In agreement with our hypothesis of predominant lateral current flow, no current was measurable without the side-contact (figure S7).

The cAFM results demonstrate that direct tunneling is possible at least up to three layers of hBN barriers (figure 2(b)). Therefore, vertical tunneling should be possible and dominant for $MoS_2$ on ML hBN, as well, and we conclude that the STS spectrum in figure 1(c) was in fact measured with a bulk hBN barrier below the ML $MoS_2$. In our heterostructure configuration, the $MoS_2$ on bulk hBN still has a lateral side-contact with graphene, which provides the necessary conductive connection at room temperature. For STS at low temperatures, where the intrinsic conductivity is frozen out, the current is rather carried by the diffusion of injected carriers, which are also called hot carriers. For positive (negative) bias above the CBM (below the VBM), electrons (holes) are injected into the CB, that need to diffuse laterally to the contact. The observed current suppression in STS (cf. figure 1(d)) on $MoS_2$/hBN at negative bias (below the VBM of $MoS_2$) points towards a less efficient diffusion of injected holes. Only at a high bias ($-3.5$ V), the hole currents increase significantly because vertical tunneling into the VBM of hBN becomes available as an additional channel. A possible scenario is that at a finite residual electron density, which is consistent with the Fermi level being located closer to the CBM, the injected holes will be minority carriers and their diffusion is limited by recombination with electrons. Another possible explanation are shallow defect states, which can effectively trap carriers at low temperatures, while being ineffective at room temperature because of thermal activation [41]. For example, oxygen passivated sulfur vacancies are abundant in $MoS_2$ [14], and they were shown to introduce a shallow defect resonance in the VBM of other structurally similar transition metal dichalcogenides, in particular $MoSe_2$ [42], without any deep in-gap state.

There is a noticeable effect of the bulk hBN decoupling layer on the defects in $MoS_2$ as well. Figure 3(a) shows a large area STM image of various point defects in $MoS_2$ on hBN. In line with previous reports on semiconducting transition metal dichalcogenides directly on graphene [16, 20], we observe different defects (panel insets) including negatively charged point defects of unknown type (*Defect A*), oxygen-passivated sulfur vacancies in the top and bottom sulfur sub-lattice (*Defects B*) and unpassivated sulfur vacancies in the top sulfur lattice (*Defect C*). In the following, we focus on unpassivated sulfur vacancies. The latter have a clear topographic fingerprint with a characteristic orbital shape, and, generally, they exhibit a deep in-gap state due to the unsaturated bonds at the defect site [14, 20, 43]. Interestingly, we find that the vacancies are charged, as suggested by the dark halo, even after decoupling $MoS_2$ with hBN [14, 18]. Figure 3(b) depicts the expected energy diagram for a negatively charged vacancy including splitting due to the Jahn–Teller effect [18, 20]. We expect three in-gap states, one unoccupied state close to the CB, one occupied state in the middle of the gap, and two degenerate occupied states near the valence band. As a reference, figures 3(c) and (d) show STS spectra across a negatively charged sulfur vacancy defect (HOMO) in $MoS_2$ directly on graphene. The pronounced upwards band bending of the CBM (indicated by the white line as guide to the eye in figure 3(d)) is consistent with the net negative charge on the defect. In agreement with other recent STM studies [18, 20], three in-gap states, assigned as $HOMO^{-1}$, HOMO and LUMO, are visible in the STS spectrum. Moreover, the defect states exhibit characteristic broadened side bands [18].

Figures 3(e) and (f) show STS spectra across an unpassivated sulfur vacancy defect in the decoupled $MoS_2$/hBN heterostructure. As mentioned before, the dark halo of the defect points towards a charged state. Indeed, the CB exhibits an upwards band bending (indicated by the white line as guide to the eye in figure 3(f)), suggesting that the investigated defect is negatively charged in this configuration as well. However, the onset of the CB is shifted to higher biases compared to $MoS_2$ directly on EG, indicating a more intrinsic nature of the $MoS_2$. Similarly, the lack of band bending for the valence band in $MoS_2$/hBN suggests that the defect can actually be brought into an overall neutral configuration, potentially due to tip-induced discharging at a large negative bias [19]. Similar to charged sulfur vacancies in $MoS_2$ directly on EG, the vacancy defect in $MoS_2$ on bulk hBN exhibits one state above the Fermi level, i.e. a LUMO state (black triangle figure 3(e)). The spectra suggest a finite broadening of the LUMO state, possibly due to phonons [18]. However, no further states are visible below the Fermi level, i.e. no HOMO states are resolved. Only at $-3.8$ V, we detect again the onset of the hBN VBM (cf. Figure 1(d) for pristine $MoS_2$/hBN). A possible explanation is that the HOMO states are experimentally not accessible because there is simply no current pathway. The bulk hBN barrier inhibits vertical tunneling and the $MoS_2$ band gap inhibits lateral transport because the HOMO level is a bound state deep inside the band gap. In this picture, it is interesting to ask if the LUMO state is in fact a strictly bound state (i.e. a deep defect [12, 44]) or if it has the character of a resonant defect state hybridizing with the CB [45]. Since the LUMO state is experimentally accessible in STS even with bulk hBN below (figure 3(f)), we conclude that the charge carriers injected from the tip escape from the localized state into the delocalized $MoS_2$ CB at a sufficient rate. Yet, the STS spectra suggest that the LUMO state (black triangle in figure 3(e)) is in fact separated from the CBM onset by a finite gap. A likely explanation is therefore that tip-induced band bending at

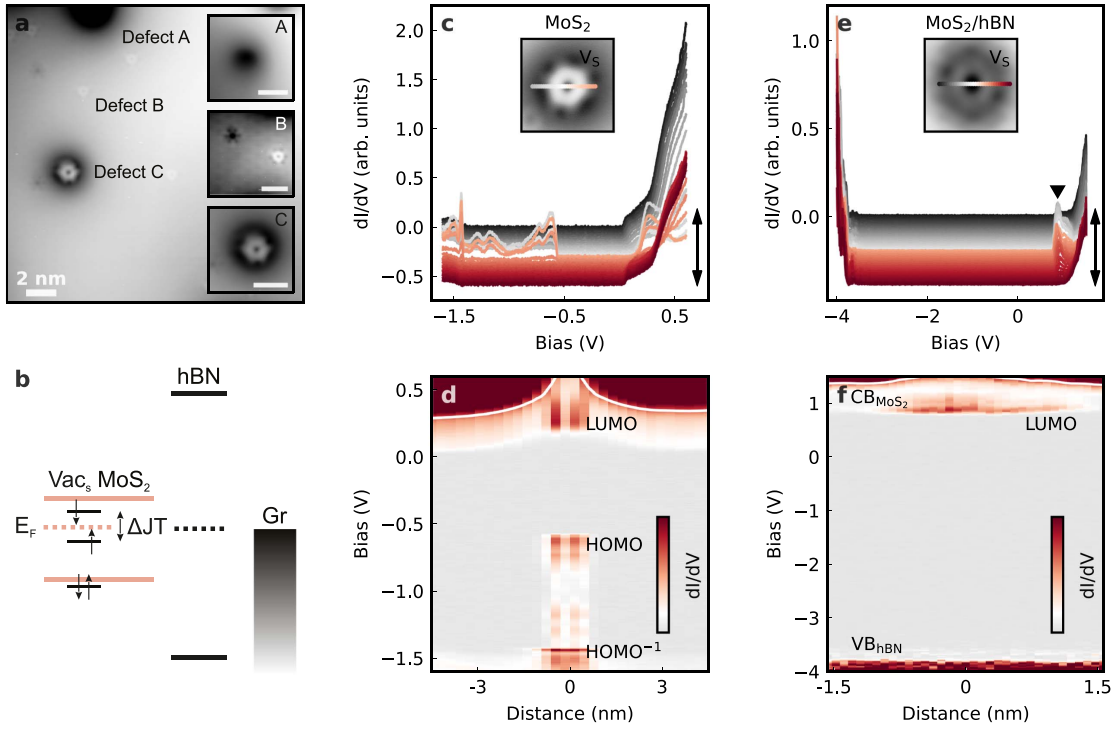


**Figure 3.** Defects in monolayer $MoS_2$. (a) Constant current STM image ($V_{bias} = 1.5$ V, $I = 30$ pA) of ML $MoS_2$ on hBN showcasing several point defects. *Defect A* is a negatively charged point defect, *defects B* are oxygen-passivated sulfur vacancies in the top and bottom layer, and *defect C* is a negatively charged sulfur vacancy. (b) Energy level scheme of the $MoS_2$/hBN/EG heterostructure with a charged sulfur vacancy exhibiting Jahn–Teller splitting ΔJT. (c), (d) STS line scans across a charged sulfur vacancy defect within a $MoS_2$/EG heterostructure. Inset: close-up STM image of the defect ($V_{bias} = 0.45$ V and $I = 100$ pA). Three defect states (HOMO$^{-1}$, HOMO and LUMO) are visible. (e), (f) STS line scans across a sulfur vacancy within a $MoS_2$/hBN/EG heterostructure. Inset: close-up STM image of the defect ($V_{bias} = 1.5$ V and $I = 30$ pA). Only the defect state above the Fermi level is visible (black triangle). The white solid lines in (d) and (f) are guides to the eye tracing the upward band bending in the CBM, which indicates a negative charge at the defect. The spatially dependent tunneling spectra are vertically offset for clarity.

positive bias enables a lateral tunneling process of the electron localized on the defect into the CB states [46, 47].

## 2. Discussion and conclusion

We investigated tunneling through monolayer $MoS_2$/few-layer hBN/graphene heterostructures by means of LT-STS and room temperature cAFM. In STS, we find indications that bulk hBN reduces the charge transfer from graphene to $MoS_2$ resulting in a Fermi level shift of −0.4 eV, such that the valence band and CB onsets of $MoS_2$ are approximately located at −1.5 V and 1.2 V, respectively, resulting in a close to intrinsic Fermi level. Somewhat counter-intuitively, spectroscopy on individual sulfur vacancies still reveals negative charging of the investigated defects. This can be understood in terms of a very long lifetime of the trapped charge at low-temperatures enabled by the thick hBN decoupling barrier, which prevents any trapped charge from tunneling into the substrate representing an effective Coulomb blockade of the defect state [48]. For the investigated side-contacted geometry, current flow in $MoS_2$ with a thick hBN tunneling barrier below occurs therefore dominantly via lateral transport, which leads to a diminished visibility of states near the valence band vs. states near the CB due to suppressed transport of holes injected from the tip. At room temperature, we find that the finite conductivity of $MoS_2$ can provide a sufficient side-contact, similar to other STS studies conducted at room temperature [30] and 77 K [49]. Therefore, the lateral current flow competes with the vertical tunneling conductivity down to few-layer hBN. Consequently, the interplay between vertical tunneling and lateral transport plays an important role for device structures with both a thin tunneling barrier and a side-contact to the semiconducting layers. This configuration is typical for gated structures, except for configurations where the semiconducting layer is electrostatically floating. For the STS experiments, one should also consider that the tip typically approaches the sample at a specific set bias until a set current is reached, which determines the distance between tip and sample. This distance is kept constant, and the bias is ramped. To favor tunneling currents over lateral transport in low-temperature STS, it may thus be advantageous to use higher current setpoints and thus smaller tip-sample distances or to eliminate the lateral contact between the semiconductor and the substrate in the heterostructure assembly.

In conclusion, the layer dependent cAFM measurements suggest that 2–3 layers of hBN may present

an optimal regime to interrogate the defect states by electronic scanning probe methods. In this regime, the $MoS_2$ is already decoupled from the underlying graphene, yet direct tunneling through the hBN is still possible, which is necessary to prevent Coulomb blockade of the defect state. In STM, the unambiguous identification of hBN barrier thickness with large exfoliated samples presents a practical experimental challenge. A recent study of defects in multilayer $WSe_2$ demonstrated that the lifetime of charged defects depends on the underlying tunneling thickness [50]. Then the width of the tunneling barrier can be extracted from the current saturation behavior at small tip-sample distances in STS [48]. The latter approach therefore provides a suitable method to determine the thickness of the hBN barrier directly in future STS experiments towards probing both electronic and many-body optical properties of the defects at their native length scale.

## 3. Methods

### 3.1. Sample preparation

Bulk crystals of hBN and $MoS_2$ were exfoliated using mechanical cleavage and the monolayers were transferred with micrometer precision onto epitaxially grown graphene on (6H)-SiC substrate. To this end, graphene was grown on (6H)-SiC wafers based on the following [51]. SiC-wafers (purchased from *University Wafer Inc.*) were diced, sonicated in methanol, and flash annealed under vacuum at 750 °C in an inductively heated reactor tube held within a graphite susceptor. Samples were then etched with a slow flow of hydrogen (0.5 SLM) in the presence of argon ($p = 1$ bar) at 1400 °C for 5 min to prepare the surface for graphene growth. Monolayer graphene samples were then grown by heating the sample to 1620 °C for 20 min under argon ($p = 1$ bar) in addition to a slow flow of argon (0.5 SLM). Samples were left to cool to room temperature after each step. Heating and cooling rates were 2 °C–3 °C per second. hBN was exfoliated onto a $Si/SiO_2$ substrate using a clear adhesive tape (*Nitto* Lensguard7568), lifted with a PC/PDMS stamp at 70 °C and placed on the sample at 180 °C in ambient atmosphere. The hBN/EG substrate was cleaned in chloroform (rt, 10 min). To achieve large exfoliated monolayers, $MoS_2$ was exfoliated using Nitto clear tape and transferred directly from the tape onto a PDMS stamp. The $MoS_2$ was subsequently released at 40 °C from the PDMS onto the hBN flake in ambient atmosphere. Finally, the whole heterostructure was cleaned in chloroform (rt, 10 min). The layer thicknesses of each material were determined afterwards. Prior to scanning probe measurements, the samples were annealed at approximately 500 K for 24 h in the preparation chamber (in ultra-high vacuum, at approximately $10^{-9}$ mbar). The annealing further reduces surface contaminants and residue from the viscoelastic transfer. The samples were stored in $N_2$-gas atmosphere after heterostructure preparation and in between the different measurements.

### 3.2. STM and spectroscopy

STM and STS measurements were conducted using a scanning probe microscope (*Createc GmbH*) at liquid helium temperatures ($T < 6$ K) and UHV ($p < 10^{-10}$ mbar) conditions. The heterostructure was located utilizing two optical ports and previously acquired optical images. The etched tungsten tip was prepared on a gold substrate. Tip stability was further verified on gold substrates for all bias voltage ranges presented. Specifically, after forming the tip, we trained the tip at a high voltage range from −4 V to 4.5 V. *A priori*, it is unknown at which exact position on the heterostructure the tip lands. Therefore, it is necessary to approach at a bias voltage above the gap of hBN (approximately 4.5 V). After a successful approach, we incrementally reduced the bias voltage in several steps. For materials with a bandgap, such as $MoS_2$ and hBN, the voltage is reduced until the smallest possible value that allows a stable tunneling current. For graphene, the bias can be reduced to values around 0 V at the setpoint of 150 pA. All STM images were acquired in constant-current mode with a bias voltage applied to the sample. Constant-height STS measurements (setpoint = 150 pA) were recorded utilizing a lock-in amplifier (frequency 683 Hz, amplitude 5 mV). Band gaps from STS were determined by applying a linear fit to the valence band edge, CB edge, and the bottom of the band gap in $\log(dI/dV)$. All STM images are presented as measured, with the exception of the inset in figure 3(e), which is filtered using a Fourier-filter.

### 3.3. Conductive atomic force microscopy

cAFM measurements were done at room temperature in an inert $N_2$-atmosphere with a commercial AFM system (*Bruker Dimension Icon*). The area of interest was first cleaned from all residues via AFM ironing by scanning over the area in contact mode with an applied force of approximately 300 nN. The minimum force sufficient to clean the surface was determined by scanning on a different flake and incrementally increasing the contact force until all residues were removed. The tip was calibrated by using a standard thermal tune tip calibration procedure. cAFM measurements were conducted in PeakForce TUNA mode using cantilevers with a nominal spring constant of 0.4 N $m^{-1}$, a force of about 1 nN and a conductive metal Cr/Au coating (Tip: *HQ:NSC19/Cr-Au*, nominal radius <35 nm). The bias voltage was applied at the sample. *IV*-curves were measured by sweeping from negative to positive bias voltages with a sweep rate of 2–6 $Vs^{-1}$.

## Data availability statement

All data that support the findings of this study are included within the article (and any supplementary files).

## Acknowledgment

We thank Johannes Figueiredo for his help with the helium ion microscopy. Work at TUM was supported by the Deutsche Forschungsgemeinschaft (DFG) via e-conversion—EXC 2089/1–390776260, the Munich Center for Quantum Science and Technology (MCQST)—EXC 2111–390814868 as well as the Munich Quantum Valley K6 and the One Munich Strategy Forum—EQAP. Work at the Molecular Foundry was supported by the Office of Science, Office of Basic Energy Sciences, of the U.S. Department of Energy under Contract No. DE-AC02-05CH11231. C K and A H acknowledge support through TUM International Graduate School of Science and Engineering (IGSSE). C K acknowledges funding through the European Union's Horizon Europe research and innovation programme under Grant No. 101076915 (2DTopS). K W and T T acknowledge support from the JSPS KAKENHI (Grant Nos. 21H05233 and 23H02052) and World Premier International Research Center Initiative (WPI), MEXT, Japan.

## Conflict of interest

The authors have no conflicts to disclose.

## ORCID iDs

J C Thomas https://orcid.org/0000-0002-2151-7725
S Levashov https://orcid.org/0009-0001-4244-8554
K Watanabe https://orcid.org/0000-0003-3701-8119
T R Kuykendall https://orcid.org/0000-0003-1362-3285
J Eichhorn https://orcid.org/0000-0003-2413-6079
A W Holleitner https://orcid.org/0000-0002-8314-4397
A Weber-Bargioni https://orcid.org/0000-0003-2986-1819
C Kastl https://orcid.org/0000-0001-5309-618X

## References

[1] Kang S, Lee D, Kim J, Capasso A, Kang H S, Park J-W, Lee C-H and Lee G-H 2020 2D semiconducting materials for electronic and optoelectronic applications: potential and challenge *2D Mater.* **7** 022003
[2] McCreary A, Kazakova O, Jariwala D and Al Balushi Z Y 2021 An outlook into the flat land of 2D materials beyond graphene: synthesis, properties and device applications *2D Mater.* **8** 013001
[3] Sarkar D, Xie X, Liu W, Cao W, Kang J, Gong Y, Kraemer S, Ajayan P M and Banerjee K 2015 A subthermionic tunnel field-effect transistor with an atomically thin channel *Nature* **526** 91–95
[4] Wang J, Sciarrino F, Laing A and Thompson M G 2020 Integrated photonic quantum technologies *Nat. Photon.* **14** 273–84
[5] Kianinia M, Xu Z Q, Toth M and Aharonovich I 2022 Quantum emitters in 2D materials: emitter engineering, photophysics, and integration in photonic nanostructures *Appl. Phys. Rev.* **9** 011306
[6] Britnell L *et al* 2012 Electron tunneling through ultrathin boron nitride crystalline barriers *Nano Lett.* **12** 1707–10
[7] Román R J P *et al* 2021 Band gap measurements of monolayer h-BN and insights into carbon-related point defects *2D Mater.* **8** 044001
[8] Hattori Y, Taniguchi T, Watanabe K and Nagashio K 2015 Layer-by-layer dielectric breakdown of hexagonal boron nitride *ACS Nano* **9** 916–21
[9] Ranjan A, Raghavan N, Holwill M, Watanabe K, Taniguchi T, Novoselov K S, Pey K L and O'Shea S J 2021 Dielectric breakdown in single-crystal hexagonal boron nitride *ACS Appl. Electron. Mater.* **3** 3547–54
[10] Lee G-H, Yu Y-J, Lee C, Dean C, Shepard K L, Kim P and Hone J 2011 Electron tunneling through atomically flat and ultrathin hexagonal boron nitride *Appl. Phys. Lett.* **99** 243114
[11] Michaelis De Vasconcellos S, Wigger D, Wurstbauer U, Holleitner A W, Bratschitsch R and Kuhn T 2022 Single-photon emitters in layered van der Waals materials *Phys. Status Solidi* b **259** 2100566
[12] Khalid S, Medasani B, Lyons J L, Wickramaratne D and Janotti A 2024 The deep-acceptor nature of the chalcogen vacancies in 2D transition-metal dichalcogenides *2D Mater.* **11** 021001
[13] Hötger A *et al* 2023 Photovoltage and photocurrent absorption spectra of sulfur vacancies locally patterned in monolayer $MoS_2$ *Nano Lett.* **23** 11655–61
[14] Mitterreiter E, Schuler B, Cochrane K A, Wurstbauer U, Weber-Bargioni A, Kastl C and Holleitner A W 2020 Atomistic positioning of defects in helium ion treated single-layer $MoS_2$ *Nano Lett.* **20** 4437–44
[15] Micevic A *et al* 2022 On-demand generation of optically active defects in monolayer $WS_2$ by a focused helium ion beam *Appl. Phys. Lett.* **121** 183101
[16] Thomas J C *et al* 2024 A substitutional quantum defect in $WS_2$ discovered by high-throughput computational screening and fabricated by site-selective STM manipulation *Nat. Commun.* **15** 3556
[17] Gupta S, Yang J-H and Yakobson B I 2019 Two-level quantum systems in two-dimensional materials for single photon emission *Nano Lett.* **19** 408–14
[18] Xiang F *et al* 2024 Charge state-dependent symmetry breaking of atomic defects in transition metal dichalcogenides *Nat. Commun.* **15** 2738
[19] Jansen D, Tounsi T, Fischer J, Krasheninnikov A V, Michely T, Komsa H-P and Jolie W 2024 Tip-induced creation and Jahn-Teller distortions of sulfur vacancies in single-layer $MoS_2$ *Phys. Rev.* B **109** 195430
[20] Aliyar T *et al* 2024 Symmetry breaking and spin-orbit coupling for individual vacancy-induced in-gap states in $MoS_2$ monolayers *Nano Lett.* **24** 2142–8
[21] Tan A M Z, Freysoldt C and Hennig R G 2020 First-principles investigation of charged dopants and dopant-vacancy defect complexes in monolayer $MoS_2$ *Phys. Rev. Mater.* **4** 114002
[22] Akkoush A, Litman Y and Rossi M 2024 A hybrid-density functional theory study of intrinsic point defects in $MX_2$ (M = Mo,W; X = S, Se) monolayers *Phys. Status Solidi* a **221** 2300180

[23] Trishin S, Lotze C, Krane N and Franke K J 2023 Electronic and magnetic properties of single chalcogen vacancies in $MoS_2$/Au(111) *Phys. Rev.* B **108** 165414
[24] Cao Q, Kreßler M, Hußmann M, Hu Y, Kusch P and Eigler S 2024 Photoluminescence modulation of graphene/$mos_2$ heterostructures separated by laser-induced functionalization *Chem. Mater.* **36** 3267–76
[25] Lorchat E *et al* 2020 Filtering the photoluminescence spectra of atomically thin semiconductors with graphene *Nat. Nanotechnol.* **15** 283–8
[26] Zhang L *et al* 2017 Electrically driven single-photon emission from an isolated single molecule *Nat. Commun.* **8** 580–7
[27] Wu S W, Ogawa N and Ho W 2006 Atomic-scale coupling of photons to single-molecule junctions *Science* **312** 1362–5
[28] Geng H, Tang J, Wu Y, Yu Y, Guest J R and Zhang R 2024 Imaging valley excitons in a 2D semiconductor with scanning tunneling microscope-induced luminescence *ACS Nano* **18** 8961–70
[29] Kaiser K, Lieske L A, Repp J and Gross L 2023 Charge-state lifetimes of single molecules on few monolayers of NaCl *Nat. Commun.* **14** 4988
[30] Klein J *et al* 2019 Impact of substrate induced band tail states on the electronic and optical properties of $MoS_2$ *Appl. Phys. Lett.* **115** 261603
[31] Li H *et al* 2024 Imaging moiré excited states with photocurrent tunnelling microscopy *Nat. Mater.* **23** 633–9
[32] Murray C *et al* 2019 Comprehensive tunneling spectroscopy of quasifreestanding $MoS_2$ on graphene on Ir(111) *Phys. Rev.* B **99** 115434
[33] Liu X, Balla I, Bergeron H, Campbell G P, Bedzyk M J and Hersam M C 2016 Rotationally commensurate growth of $MoS_2$ on epitaxial graphene *ACS Nano* **10** 1067–75
[34] Zhang C, Chen Y, Johnson A, Li M-Y, Li L-J, Mende P C, Feenstra R M and Shih C-K 2015 Probing critical point energies of transition metal dichalcogenides: surprising indirect gap of single layer $WSe_2$ *Nano Lett.* **15** 6494–500
[35] Zhang Y, Brar V W, Wang F, Girit C, Yayon Y, Panlasigui M, Zettl A and Crommie M F 2008 Giant phonon-induced conductance in scanning tunnelling spectroscopy of gate-tunable graphene *Nat. Phys.* **4** 627–30
[36] Pielić B, Mužević M, Novko D, Cai J, Bremerich A, Ohmann R, Kralj M, Šrut Rakić I and Busse C 2024 Probing the interplay of interactions, screening and strain in monolayer $MoS_2$ via self-intercalation *npj 2D Mater. Appl.* **8** 61
[37] Rosenberger M R, Chuang H-J, McCreary K M, Hanbicki A T, Sivaram S V and Jonker B T 2018 Nano-"squeegee" for the creation of clean 2D material interfaces *ACS Appl. Mater. Interfaces* **10** 10379–87
[38] Li R, Taniguchi T, Watanabe K and Xue J 2020 Detecting band profiles of devices with conductive atomic force microscopy *Rev. Sci. Instrum.* **91** 073702
[39] Velický M *et al* 2020 Electron tunneling through boron nitride confirms marcus-hush theory predictions for ultramicroelectrodes *ACS Nano* **14** 993–1002
[40] de Araújo D B *et al* 2020 Controlling the electronic bands of a 2D semiconductor by force microscopy *2D Mater.* **7** 045029
[41] Goodman A J, Willard A P and Tisdale W A 2017 Exciton trapping is responsible for the long apparent lifetime in acid-treated $MoS_2$ *Phys. Rev.* B **96** 121404
[42] Barja S *et al* 2019 Identifying substitutional oxygen as a prolific point defect in monolayer transition metal dichalcogenides *Nat. Commun.* **10** 3382
[43] Schuler B *et al* 2019 Large spin-orbit splitting of deep in-gap defect states of engineered sulfur vacancies in monolayer $WS_2$ *Phys. Rev. Lett.* **123** 76801
[44] Khalid S, Janotti A and Medasani B 2024 Role of chalcogen vacancies and hydrogen in the optical and electrical properties of bulk transition-metal dichalcogenides *2D Mater.* **11** 031003
[45] Aghajanian M *et al* 2020 Resonant and bound states of charged defects in two-dimensional semiconductors *Phys. Rev.* B **101** 081201
[46] Teichmann K, Wenderoth M, Loth S, Ulbrich R G, Garleff J K, Wijnheijmer A P and Koenraad P M 2008 Controlled charge switching on a single donor with a scanning tunneling microscope *Phys. Rev. Lett.* **101** 076103
[47] Schofield S R, Studer P, Hirjibehedin C F, Curson N J, Aeppli G and Bowler D R 2013 Quantum engineering at the silicon surface using dangling bonds *Nat. Commun.* **4** 1649
[48] Zhang R, Clark G, Xu X, Darancet P T and Guest J R 2021 Observation of single-electron transport and charging on individual point defects in atomically thin $WSe_2$ *J. Phys. Chem.* C **125** 14056–64
[49] Tilak N, Li G, Taniguchi T, Watanabe K and Andrei E Y 2023 Moiré potential, lattice relaxation, and layer polarization in marginally twisted $MoS_2$ bilayers *Nano Lett.* **23** 73–81
[50] Bobzien L *et al* 2024 Layer-dependent charge state lifetime of single Se vacancies in $WSe_2$ (arXiv:2407.04508v1) pp 1–17
[51] Emtsev K V *et al* 2009 Towards wafer-size graphene layers by atmospheric pressure graphitization of silicon carbide *Nat. Mater.* **8** 203–7